

Content-Aware Point Cloud Simplification of Natural Scenes

Reuma Arav¹, Sagi Filin¹, and Norbert Pfeifer²

Abstract—Laser scanning technology is becoming ubiquitous in studies involving 3-D characterizations of natural scenes, e.g., for geomorphological or archeological interpretations. Setting the point density in such scanning campaigns is usually dictated by the objects of interest within the site yet is applied to the entire scene. Such campaigns result in large data volumes, which are difficult to analyze and where the objects of interest may be hidden in the redundant data. To reduce these excessive volumes, existing simplification strategies maintain smoothness and preserve discontinuities in the point cloud but disregard the need to preserve detail at the regions of interest (ROIs). To address that, this article proposes a new, context-aware, subsampling approach that retains the high resolution of objects of interest while reducing the data load of less important regions. To do so, we identify the ROI by means of visual saliency measures and reduce the data volume only at the nonsalient regions. To facilitate progressive subsampling, the reduction is based on a hierarchical data structure that is surficial in nature. In this way, the retained representative points describe the underlying surface rather than an interpolation of it. We demonstrate our proposed model on datasets originating from different scanners that feature a variety of scenes. We compare our results to three common simplification approaches. Our results show a reduced point cloud that is similar to the original and allows analysis of ROI at the required point resolution, regardless of the level of simplification.

Index Terms—Ball tree, point cloud, reduction, simplification, subsampling, visual saliency.

I. INTRODUCTION

LASER scanned 3-D point clouds have become an invaluable ingredient in support of a variety of applications, including urban planning, archeology, cultural heritage, ecology, and geomorphology (e.g., [1], [2], [3], [4], [5], [6], [7], [8]). The eventual utilization of the 3-D clouds dictates the point density during acquisition and is then applied to the entire scene. As an example, to extract buildings within urban regions, Guo *et al.* [9] used scans with up to 40-pts/m² density, though only the building boundaries benefit from such

a resolution. A similar density of 40 pts/m² was also set to scan and analyze rockfall activity [5], and a density of 2000 pts/m² was applied to monitor paleolithic archeological excavations [4]. Valuable as such densities may be for the entities of interest, and in natural scenes, much of the recorded data relates to the surrounding surface rather than the objects of interest. The outcome is an inflated data volume that makes downstream applications, such as registration, change detection, or surface reconstruction, difficult and unmanageable [10], [11]. Moreover, the redundancy of the data may also hide the regions of interest (ROIs) at certain scale levels.

To make processing accessible, it is customary to first simplify the data by reducing its volume. In that respect, mesh-based methods were initially proposed. Following the construction of an irregular mesh, redundant cells were removed according to a predefined criterion. As an example, Luebke *et al.* [12] used mesh compression to simplify the point cloud. In [13], a group of triangles was selected to be simplified based on the angle between them. The authors then iteratively simplified the selected group by recomputing a Delaunay triangulation under specific constraints (e.g., triangle area, angle between neighboring triangles) and then rechose the triangles. In [14], a Poisson disk was proposed to sample points on the triangles. However, as noted in [15] and [16], mesh-based approaches come with high computational cost for the initial mesh construction, especially in large point clouds. Moreover, the quality of the simplification relies heavily on the initial mesh, which usually requires further tuning.

To alleviate the need for computationally intensive preprocessing, direct approaches suggest working on the raw data. Common approaches divide the point cloud into uniform spatial cells and sample the data so that only a single point is left within each one [17], [18], [19]. This spatial uniformity does not correspond to the underlying surface features and leads to loss of vital details and to a wrongful depiction of the scene (see Fig. 1). To remove redundant points while maintaining important features, researchers turn to study either shape- or point-based simplification methods. Shape-based approaches follow the notion that some structures can be simplified by resampling points using an explicit equation of their parametric form, based on different reduction schemes. As an example, in [20], a quadtree data structure was employed so that points that are part of a plane were reduced by keeping a single child node for each parent. In [21], only points that define a “concave hull” of a plane were retained. Lin *et al.* [22] resampled points using a fit plane equation to the original points. Zhang *et al.* [16] extended the resampling process to

Manuscript received 30 June 2022; revised 20 August 2022; accepted 16 September 2022. Date of publication 21 September 2022; date of current version 7 October 2022. This work was supported in part by the European Union’s Horizon 2020 Research and Innovation Programme under the Marie Skłodowska-Curie Grant 896409 and in part by TU Wien Bibliothek through the Open Access Funding Programme. (Corresponding author: Reuma Arav.)

Reuma Arav is with the Department of Geodesy and Geoinformation, Technische Universität Wien, 1040 Vienna, Austria (e-mail: reuma.arav@geo.tuwien.ac.at).

Sagi Filin is with the Department of Civil and Environmental Engineering, Technion—Israel Institute of Technology, Haifa 32000, Israel.

Norbert Pfeifer is with the Department of Geodesy and Geoinformation, Vienna University of Technology, 1040 Vienna, Austria.

Digital Object Identifier 10.1109/TGRS.2022.3208348

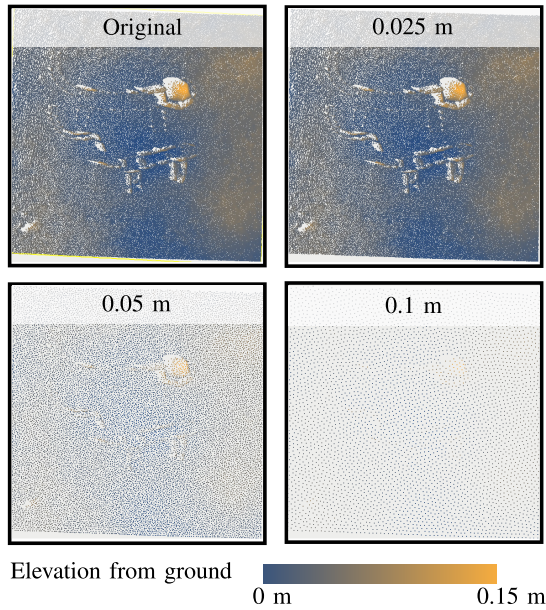


Fig. 1. Demonstrative application of a common point cloud reduction algorithm using different radii (here using [19]). As the downsampling radius reaches 0.05 m, the entities that were the focus of the scan disappear.

include simplification rules for cylinders and spheres. Still, such approaches require special adaptation to natural scenes, as parametric objects are uncommon there.

Achieving generality, direct point-based approaches have aimed to reduce points according to a definition of their importance. Leal *et al.* [10] proposed to evaluate the importance of each point according to its curvature. High curvature points were retained, while the rest were subsampled so as to achieve a minimal distance between the subsampled cluster points and the original cloud. Li *et al.* [23] also defined high curvature points as important. The authors computed the curvature values by differentiating between a point's normal and that of its surroundings. Ji *et al.* [15] evaluated a point's importance by a set of geometric features, such as normal vector difference, projection distance, and spatial distance. Important points were retained, while unimportant ones were reduced using an octree data structure. Gong *et al.* [24] kept feature points defined as an edge- or high-curvature-related points, while nonfeature points were resampled over a Delaunay triangulation. Entropy was also used for evaluating point importance. Xuan *et al.* [25] computed the entropy of the angles between neighborhood normals and a locally fit plane. The higher the entropy, the more important the point. The simplification stage was iterative: at each iteration, the least important point was removed, the neighborhoods were updated, and the importance was recomputed. The simplification terminated when the specified number of points in the cloud was reached. In [11] and [26], the point clouds were clustered at first, and then, the entropy of each cluster's curvature was estimated. Only points with entropy higher than that of the cluster were kept.

While existing methods focus on maintaining key features, they do not consider the context of the acquired point cloud. Therefore, the reduction is also applied to ROIs, even

when they are scanned in higher detail for further analysis (c.f. Fig. 1). In this article, we propose a content-aware solution to the point simplification problem. Inspired by the human visual system, which works as a filter to allocate more attention to pertinent regions, we utilize visual saliency to maintain ROIs, while we simplify others. This is carried out by using a hierarchical proximity strategy that captures the actual distribution of the points in 3-D space. The resulting simplification process focuses on important regions while promising a reduction that is geometrically more similar to the original one. We demonstrate the applicability of the proposed method on four different datasets acquired by two types of laser scanning platforms. We show that the proposed saliency-based simplification produces a simplified cloud that has similar geometric properties as the original one. The reduced point cloud not only maintains the geometric characteristics of the surface but also highlights regions with high visual attention while reducing others. In this way, areas of interest that may have been hidden by the excessive point data are coming to light.

II. METHODS

Motivated by theories associated with visual attention, our simplification model is governed by the detection of salient regions. Our objective is to preserve the density therein and downsample the rest of the point cloud. To facilitate progressive subsampling, we introduce a distance-driven data-aware hierarchical structure, from which points are sampled. As a consequence, the simplification process is partitioned into two main parts: 1) the evaluation of saliency, which is based on geometric surface features (Section II-A), and 2) the downsampling phase, which is based on a designated data structure we propose (Section II-B). The model was developed and implemented in Python 3.8 and is openly available online [27], except for certain parts that require third-party software (details given in the following).

A. Surface Features and Saliency Estimation

In natural scenes, the entities of interest are embedded within the topography. They may exhibit a sharp transition in reference to the surrounding surface, e.g., gullies or crevasses, or transition smoothly (such as bulbous rocks or mounds), making the definition of their edge vague (c.f. [28], [29], [30] for further discussion of vagueness). To trace such embedded entities, the use of first-order features, which essentially seeks strong curvature values, is likely to fail with the latter class. The utilization of second-order features, which seeks strong changes in curvature values, may help identify variations around smoother object-to-background transitions. However, it is likely to highlight only boundary points rather than the object itself. Therefore, first-order methods are insufficiently sensitive, and second-order ones may yield partial results.

Our aim here is to focus and preserve the entities themselves rather than their boundary. To highlight them, we consider the entities salient with respect to their surrounding and search for geometrical surface features that can trace these entities in their entirety. To do so, we deviate from the traditional

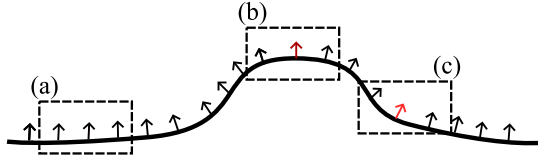


Fig. 2. Saliency computation of a continuous surface. The saliency of the center point in each neighborhood is being estimated. In neighborhood (a), normals and curvature are approximately the same leading to nonsalient center point; in neighborhood (b), the normals are different, but curvature is similar, leading to a higher saliency value. (c) Both normals and curvature differ from their neighborhood—highest saliency value is reached.

detection scheme. Assuming that pertinent regions differ from their surroundings, we follow the neurological center-surround principle, which asserts that neurons in the retina are more sensitive to regions that stand out from their surroundings [31], [32], [33]. Accordingly, a center-surround operator, which measures the deviation between a point and its surrounding, is being used. As the surface is continuous and smooth, the change is unlikely to occur within the immediate neighborhood of a point, but rather in reference to farther regions [34]. Therefore, we utilize a weighting function that assigns points near the center with lower weights, while higher values are given to those of the surrounding regions. The assignment of the weights is dictated by a Gaussian-form-based radial function whose center is at ρ (minimal object size) and σ controls the breadth of the surrounding

$$\mathcal{W}_{ij}(x_i - x_j) = \frac{1}{\sigma\sqrt{2\pi}} e^{-\frac{1}{2}\left(\frac{\|x_i - x_j\|_2 - \rho}{\sigma}\right)^2}. \quad (1)$$

Under such a setup, the center point has a weight of zero, while the maximal is at ρ . Setting ρ and σ according to the minimal size of the entities in the scene, we measure

$$\begin{aligned} d\mathbf{n}_i &= \frac{1}{K} \sum_{j=1}^K \mathcal{W}_{ij} \cdot (\mathbf{n}_i - \mathbf{n}_j) \\ d\kappa_i &= \frac{1}{K} \sum_{j=1}^K \mathcal{W}_{ij} \cdot (\kappa_i - \kappa_j) \end{aligned} \quad (2)$$

where K is the neighborhood size and n_i and κ_i are the estimated normal and curvature at point i , respectively. Both $d\mathbf{n}$ and $d\kappa$ measure the respective weighted mean difference in normal and curvature between the surrounding surface and the analyzed point @ $_i$. Fig. 2 shows the geometric meaning of the saliency computation.

We normalize and address the unit difference by an exponential normalization of both measures, leading the saliency to be given by

$$S_i = 2 - [\exp(-d\mathbf{n}_i)) + \exp(-d\kappa_i)]. \quad (3)$$

Note that textured areas and the effect of measurement noise are expressed in low variance by the saliency measures. Therefore, the variances of $d\mathbf{n}$ and $d\kappa$ are tested statistically for each point using the χ^2 -test. Statistically insignificant responses are marked as zero and are not considered in the overall saliency estimation.

We adopt the principal component analysis (PCA) method for normal estimation. Given a point \mathbf{q} and its set of k nearest

neighbors \mathbf{p} , such that $\mathbf{p}_i \in \mathbf{p}$, we define $\bar{\mathbf{p}}_i = \mathbf{p}_i - \mathbf{q}$ and the covariance matrix, \mathbf{C} , by

$$\mathbf{C} = \frac{1}{k} \sum_{i=1}^k \bar{\mathbf{p}}_i \cdot \bar{\mathbf{p}}_i^T; \quad \mathbf{C}\mathbf{v}_j = \lambda_j \mathbf{v}_j, \quad j \in \{1, 2, 3\} \quad (4)$$

where \mathbf{v}_j and λ_j are the eigenvector and values, respectively. As \mathbf{C} is positive semidefinite ($0 \leq \lambda_3 \leq \lambda_2 \leq \lambda_1$), we have \mathbf{v}_3 , corresponding to λ_3 , as the estimate of n_q , the surface normal. To disambiguate the normal sign, all normals are oriented toward a single viewpoint, \mathbf{v}_p , such that

$$n_q = \begin{cases} n_q, & \text{if } n_q \cdot (\mathbf{v}_p - \mathbf{q}) \geq 0 \\ -n_q, & \text{otherwise.} \end{cases} \quad (5)$$

Curvature estimation is less forward, as there is no convention to its estimation within point clouds. In [34], we have shown that a nonparametric curvature estimation describes the change of the surface in an efficient way. This is achieved by quantifying the convexity of the surface at each point according to the characteristics of the points' distribution around it. Specifically, the nonparametric curvature is computed as the sum of the projections of neighboring points on \mathbf{n}^q , i.e.,

$$\kappa = \frac{1}{k} \sum_{i=1}^k n_q^T \bar{\mathbf{p}}_i. \quad (6)$$

Points whose distribution around \mathbf{q} is uneven, e.g., at the scan edges or near occluded areas are considered nonviable. These are eliminated by projecting the neighborhood points to the tangent plane at \mathbf{q} and analyzing the barycenter deviation from \mathbf{q}

$$d\mathbf{q} = \frac{1}{k} \sum_{i=1}^k (\mathbf{I} - n_q n_q^T) \bar{\mathbf{p}}_i. \quad (7)$$

A lower response-level bound σ_κ is estimated directly from the measurement accuracy m_0 , i.e., $\sigma_\kappa = m_0$. Assuming normal distribution, i.e., $N \sim (\varepsilon, \sigma_\kappa)$, we establish a Z-test to determine whether the computed curvature is statistically insignificant. In this way, only significant estimates are assigned with a nonzero curvature value.

Curvature and saliency values were both computed using a designated code developed for the purpose (openly available at [27]; some parts are using OPALS [35], a third-party licensed software).

B. Point Cloud Simplification

Two approaches can be applied for the point cloud simplification: one is driven by the reduction rate (or the number of points) and the other is directed by the desired distance between neighboring points. Motivated by the idea that salient regions stand for important objects and should maintain their resolution, such regions are not to be reduced. As the reduction rate relies on the number of salient points and cannot be set in advance, we prefer a distance-based simplification approach. Normally, under this framework, the data are divided into cells based on the desired distance and then reduced by choosing one representative point from each cell (e.g., [15], [18], [19]). Though voxel-grid and octree data structures are

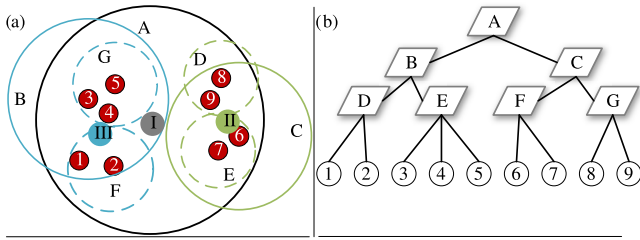


Fig. 3. Ball tree data structure: (a) partitioning of the data; Circle “A” holds all the points, whose centroid is at I. It is then divided into “B” and “C,” whose centers are at points 6 and 5. These cells are also subdivided to circles D–F. (b) Tree hierarchy representation, corresponding to the division in (a).

usually used as partitioning schemes for the simplification process, we adopt a ball tree representation [36]. In such a scheme, the point cloud is partitioned into subsets that correspond to the scanned, surficial, elements. Based on the proximity, the ball tree is a binary structure that maintains spatial data hierarchically. Each node in the tree defines a region that consists of all the points bounded by a hypersphere (in fact, a plane). Its interior child nodes are chosen so that the distance between the two nodes is maximal. Construction of the tree is performed iteratively for each cell, where at each iteration, the centroid of the point set is computed. For example, the first centroid in the first iteration of the dataset presented in [Fig. 3(a)] is gray point I. The farthest point from this centroid is set as the center of the first child (point #6). The second child is set at the farthest point from the first point (point #3). Points are then assigned to each child node by their proximity (circles B and C). Note that the sphere lines can intersect each other, but the points must be clearly assigned to one cluster. The hierarchical subdivision achieves nodes with decreasing size as the node-level increases (circles D–G). The number of points per node level varies based on their distribution. In our example, “A” holds all the points, “B” holds points 1–5, “D” holds points 8 and 9, and so on [Fig. 3(b)].

As such, trees capture the actual distribution of the points in their native space, and querying might be significantly more efficient [36]. Being distance-driven rather than coordinate, the proposed data structure is invariant to translation and rotation, a particularly important property when the data are acquired by terrestrial laser scanners. Note also that balancing the number of points per node is not prioritized as there is no constraint on the number of points per node. This is a welcome property as it suggests that the subsampling becomes less affected by the varying density within the scan. Since the node level corresponds to the area covered, choosing a point from each cell at a certain level would be equivalent to sampling at the corresponding distance.

Assuming that salient points belong to ROIs, cells that include at least 60% of such points are kept untouched. Cells with nonsalient points are reduced to one representative point. Reduction is also carried for cells with zero saliency points. In this way, we ensure that reduction will be performed when there are no salient points in the dataset. Wishing to follow the original point cloud, this point should represent the cell with the least deviation from the original points. It is common to use

the averaged point in each cell (e.g., [18], [19]). However, this inserts a deviation from the original point position. Avoiding such modifications to the cloud, the chosen representative point is the closest point to the average of all nonsalient points in the cell. In this way, the representative point is chosen from the original point cloud without introducing a different point. In fact, as the ball tree retains shape-related surface properties, the chosen point represents the surface covered by the cell.

The distinction between salient and nonsalient points is decided by considering them as arriving from two different distributions, which can be separated by clustering; otherwise, it is considered “nonsalient” and will be reduced.

The ball-tree data structure was created using the Python package *scikit-learn* v.0.23.2 [37] using a leaf size of 40 points for all datasets. The downsampling procedure is independent of the saliency and curvature computation and is openly available at Arav [27].

C. Evaluation

For the evaluation, we use three baseline methods for comparison.

1) *Mesh-Based*: Samples are uniformly pregenerated over a mesh version of the point cloud. From these, a sample is randomly selected and all samples within a sphere of r are removed, while the selected sample remains [14]. We used MeshLab [38, v2020.03+dfsg1] to generate the downsampled datasets.

2) *Voxel-Based*: The 3-D space is divided into a voxel grid of size r . From each cell, only the averaged point remains (e.g., [18], [19]). This method was executed using the Python package *open3d* v.0.13.0 [18].

3) *Point-Based Curvature-Aware*: Specifying a distance r for low curvature values and 0 for high curvature values, points are being picked from the original cloud. This is done so that no point is closer to another point than the linearly interpolated spatial distance. Therefore, regions with higher curvature values are retained, while others are reduced to the averaged point in each cell. This approach was executed in CloudCompare v2.11.1 [19] using the nonparametric curvature computed for the saliency estimation (Section II-A).

Evaluation of the models was carried out by means of both visual inspection and by a set of quantitative measures performed against the original datasets. We used four metrics to quantify the results. The first refers to the eventual reduction rate and the other three measure the geometric distortion between original and simplified point clouds as follows.

4) *Cloud-to-Cloud Distance*: Here, we measure the shift between the simplified cloud and the original. This is computed by two-sided cloud-to-cloud (C2C) distances. Given the points $a_j \in \mathbf{A}$ in the original point cloud and $b_i \in \mathbf{B}$ in the simplified cloud, the C2C distance is computed by

$$d_{\mathbf{A},\mathbf{B}}^{\text{C2C}} = \text{mean} \left(\frac{1}{N_{\mathbf{A}}} \sum_{\forall a_j \in \mathbf{A}} \|E(i, j)\|^2, \frac{1}{N_{\mathbf{B}}} \sum_{\forall b_i \in \mathbf{B}} \|E(j, i)\|^2 \right) \quad (8)$$

where $E(i, j)$ is the error vector between a_j and the closest point $b_i \in \mathbf{B}$, $E(j, i)$ is the error vector from a point b_i to

TABLE I
PROPERTIES OF THE DATASETS USED IN THE STUDY

	Data type	Coordinates (lat./long.)	Number of points	Point density [pts/m ²]	Extent [m × m]	Scanner type
# I	Flat terrain	31°22′/35°24′	1,632,928	8.5 ± 5.5 [†]	480 × 370	ALTM 2050*
# II	Alpine terrain	46°52′/10°44′	268,161	25.3 ± 8.6	90 × 80	VUX-1UAV**
# III	Arch. site	29°57′/34°58′	224,186	17,040 ± 6,550	3.5 × 3.5	c10***
# IV	Cave	47°57′/15°42′	786,267	6,675 ± 1,100	4.7 × 5.4 [‡]	VZ2000**

[†] This dataset have two distinct regions that hold higher density (due to strip overlapping).

[‡] The cave ceiling height is 2.7 m.

* Optech Inc.

** Riegler Laser Measurement Systems GmbH.

*** Scanstation c10, Leica Geosystems AG.

its closest point $a_j \in \mathbf{A}$, and $N_{\mathbf{A}}$ and $N_{\mathbf{B}}$ are the number of points in \mathbf{A} and \mathbf{B} , respectively [39].

5) *Cloud-to-Plane Error*: The cloud-to-plane (C2P) metric penalizes according to the points' distance from the local plane and is computed by

$$d_{\mathbf{A},\mathbf{B}}^{C2P} = \frac{1}{N_{\mathbf{A}}} \sum_{\forall a_j \in \mathbf{A}} [E(i, j) \cdot \mathbf{n}_j]^2 \quad (9)$$

where \mathbf{n}_j is the normal vector of point a_j [39].

6) *Deviation of the Normals*: A good simplification method retains the estimated normals following the reduction. This deviation is evaluated by averaging the function of the angle between normals of corresponding points

$$e_{\mathbf{A},\mathbf{B}}^{\text{DoN}} = \frac{1}{N_{\mathbf{A}}} \sum_{\forall a_j \in \mathbf{A}} (1 - \mathbf{n}_i \cdot \mathbf{n}_j) \quad (10)$$

where \mathbf{n}_i is the normal at point b_i . Here, we use the nearest neighbors within a specified radius, found via the ball-tree data structure. This metric also eliminates the inherent disadvantage of the baseline methods in using the mean point as a representative point rather than the original.

III. RESULTS

We demonstrate the application of our saliency-based approach on datasets acquired by airborne and terrestrial platforms. Each dataset features different point density and presents a different set of entities, pronounced or subtle (Table I and Fig. 4).

We applied each of the baseline methods (Section II-C) and the proposed saliency-based reduction to every dataset at four levels of simplification. For the airborne scans, we used the sampling distance r of 1, 2, 5, and 10 m. As for the terrestrial datasets, these were both reduced to sampling distance r of 0.05, 0.1, 0.5, and 1 m.

A. Dataset #I—Flat and Disturbed Terrain

The first dataset is an airborne laser scan acquired over the Ze'elim alluvial fan, Israel (see Fig. 4(a) and [40, Table I]). This region has been the focus of geomorphological study over the past few years, mostly due to the accelerated landform

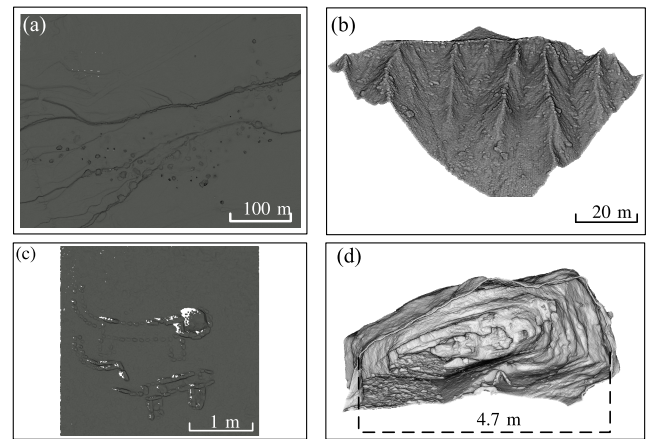


Fig. 4. Shaded reliefs of the studied point clouds. (a) Dataset #I—flat and disturbed terrain. (b) Dataset #II—Alpine terrain. (c) Dataset #III—open-air archeological site. (d) Dataset #IV—cave. Each dataset presents a different set of challenges.

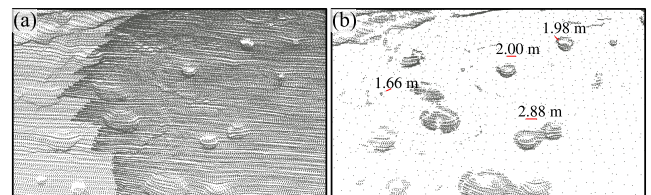


Fig. 5. Dataset #I (flat terrain): A closer look at regions with overlapping scanlines (a) before and (b) after simplification at a 2-m sampling distance. The average distance between points corresponds to the simplification distance.

processes that control the fan (e.g., [41], [42], [43], [44], [45]). Gullies dissect the relatively flat surface of the fan at changing depths and widths (2–6 and 5–9 m, respectively), while sink-holes puncture it with depressions of varying diameters and depths (4–20 and 0.5–4.5 m, respectively). The average point density is 8.5 pts/m² with a standard deviation of 5.5 pts/m². However, due to areas with overlapping scanlines, the density varies abruptly from 10 ± 1.0 to 5 ± 0.5 pts²/m. An example for such a change is presented in [Fig. 5(a)].

Being generally flat, the fan surface can be described reliably with less points per square meter. However, the

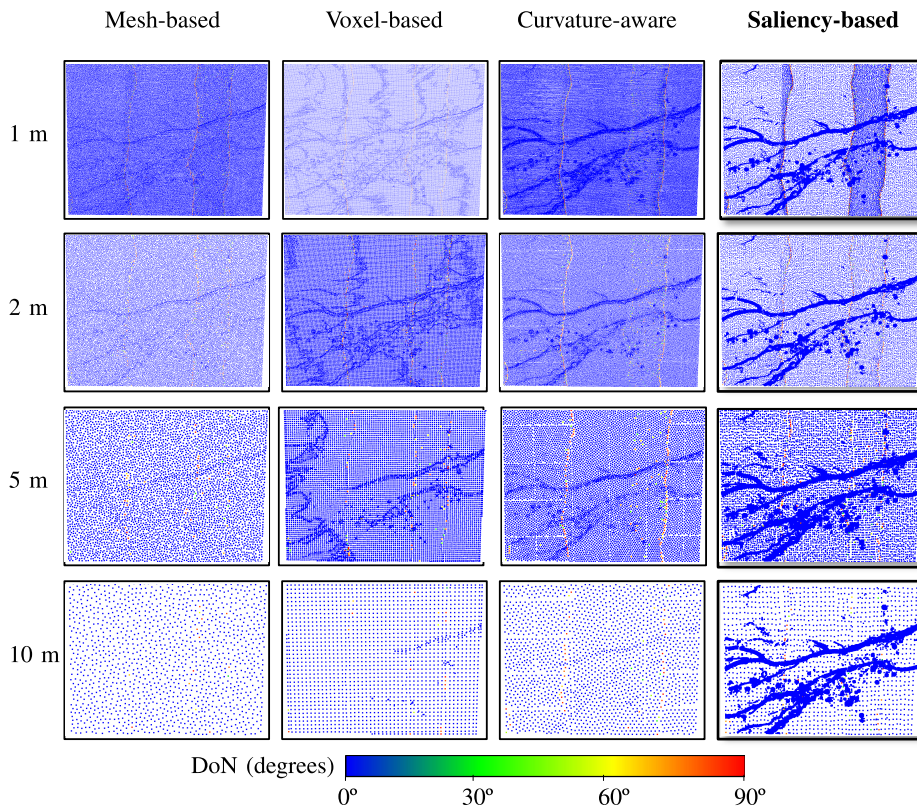


Fig. 6. Simplified point clouds of dataset #I (flat terrain) using different methods and sampling distances. Colors represent the angle of normal deviation from the original cloud.

geomorphological features contain structural details, such as side collapses, which require higher resolution documentation. The versatile types of features in the scan, as well as the high variability in point densities, pose a challenge in setting a uniform distance-based simplification criterion. This can be seen in the application of the mesh- and voxel-based simplifications, which are driven by uniform sampling (Fig. 6), where sinkholes are largely removed from the dataset at 1–2-m sampling distances, whereas at 5- and 10-m gullies, they also cleared away. Application of the curvature-aware approach yields better visual results, especially at 2 m. However, at the higher simplification levels of 5 and 10 m, most entities disappear as well.

In the proposed simplification method, saliency was computed with 2-m minimal object size, based on 0.5-m-radius neighbors for surface features estimation (Fig. 7). Following the simplification step, the entities are captured at all levels of simplification, while the fan surface is described in less detail. This is achieved while maintaining the predefined distance at nonsalient regions [Fig. 5(b)]. The simplification is unaffected by the changing resolutions in the scans. This can be seen in the seamline that has disappeared after the reduction (see Fig. 5 as an example).

Fig. 6 also shows the deviation of the normals (DoN) error distribution within the data for the utilized methods. It reveals that in all four methods, the largest errors were along the seamlines of the lower and higher resolutions. Obviously, there are some small geometric discrepancies, which lead, together

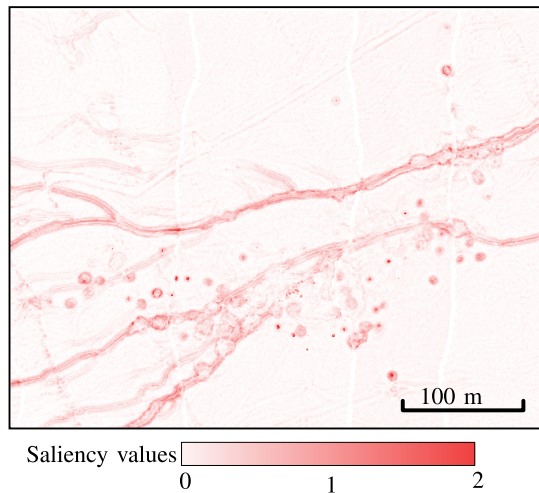


Fig. 7. Saliency estimation for dataset #I (flat terrain).

with very high point density, to wrongly estimated normals in the original point cloud.

A quantitative analysis shows that the reduction rate of the proposed method is lower than in other approaches (Fig. 8 and Table II). Still, it achieves the highest similarity to the original cloud in most reduction levels. This is evident in the lower C2P and C2C distances, as well as in the low DoN angles. The mean C2P distance for the saliency-based method at a 10-m sampling distance reaches 0.5 m, compared

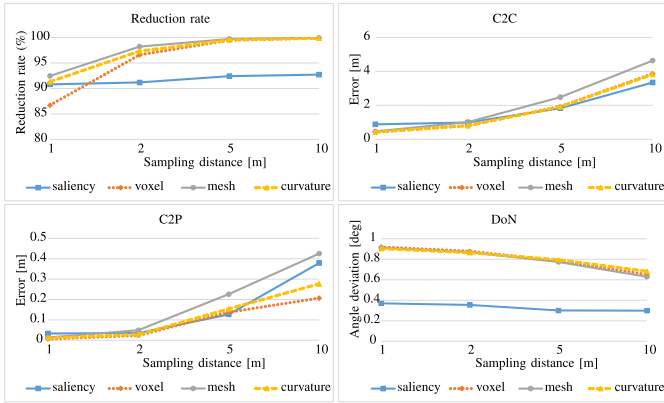


Fig. 8. Quantitative analysis of the simplification methods in different sampling distances in dataset #I (flat terrain). The graphs of the C2C and C2P errors present the mean value of all errors; the DoN graphs show the median value.

TABLE II

NUMBER OF POINTS REMAINING IN DATASET #I (FLAT TERRAIN) AFTER REDUCTION AT EACH SIMPLIFICATION LEVEL, FOR EACH METHOD USED

Sampling distance [m]	1	2	5	10
Saliency-based	150,131	144,027	123,775	118,979
Mesh-based	123,117	28,946	4,798	1,355
Voxel-based	216,641	55,401	8,671	1,965
Curvature-aware	141,835	43,364	7,640	1,935

to 6.5, 4.0, and 3.6 m, for the mesh-, curvature-, and voxel-based simplifications, respectively. The estimated normals in the saliency-based simplified cloud differ by up to 0.35° from the original estimations, irrespective of the downsampling distance. These values are at least 0.5° lower than the DoN in the other approaches.

B. Dataset #II—Alpine Terrain

The second dataset was acquired by a helicopter at Upper Kaunertal, Austria (see Fig. 4(b) and [46, Table I]). Contrasting dataset #I, the present one features a mountainous terrain with topographic variations and a general slope of 70%. The dataset consists of ridges and wide gullies (approximately 13 m wide) whose banks rise up to 8 m above their thalweg. In addition, rocks at various sizes are spread along the slopes [Fig. 4(b)]. Application of the three baseline simplification methods at 1- and 2-m sampling distances retains the main characteristics of the surface (Fig. 9). On the higher levels of reduction (i.e., 5 and 10 m) hardly, any points remain (Table III). Of them, the voxel-based method produced clouds with the most points: 543 at a 5 m and 140 at a 10-m sampling distance. At such a level of reduction, no features or surfaces are depicted.

Saliency values were computed with 1- and 1.5-m minimal object sizes, based on 0.15-m-radius neighbors for surface

TABLE III
NUMBER OF POINTS REMAINING IN DATASET #II (ALPINE TERRAIN) AFTER REDUCTION

Sampling distance [m]	1	2	5	10
Saliency-based	46,940	44,775	43,204	42,961
Mesh-based	5,912	1,273	203	51
Voxel-based	11,932	3,091	543	140
Curvature-based	7,788	2,147	365	93

features estimation (Fig. 10). It clearly shows that with smaller object sizes, the ridges are more confined, while larger entities (e.g., gullies) are not highlighted. As we wish to keep the gullies as well, the downsampling was carried out using the 1.5-m minimal object size. The application of the proposed method produces simplified clouds that are similar to the original, without affecting the topography characteristics. This is clearly evident in the C2C, C2P distances, as well as in the DoN angles (Fig. 11). For both C2C and C2P, the saliency-based approach shows the lowest distances to the original cloud. As for the DoN values, all simplification methods show high discrepancies. The saliency-based approach leads to DoN values that are between 13° and 15° , as opposed to 15° – 22° in the other simplified clouds. The inconsistency of the surface, as well as the large variability of the salient morphological features, leads to low reduction rates of the proposed method where 42961 points remaining at a 10-m sampling distance, out of the original 268 161 (Table III). This allows further geomorphological analysis, unlike the other simplified clouds.

C. Dataset #III—Open-Air Archeological Site

The third dataset is a terrestrial laser scan taken from a single position. It documents an open-air archeological site in Uvda Valley, Israel (Fig. 4(c) and Table I). The scan records two animal-like figures made of small stones (mostly 0.01–0.05 m high) affixed to the ground. The surface around the specimen is relatively flat. Therefore, it is possible to represent it with far fewer points, without affecting its description. However, due to the small size of the artifact's stones, the uniform sampling of 0.05 m is likely to remove them from the data. This can be seen when applying the mesh-based method at such a distance (Fig. 12). Note that the voxel-based simplified cloud does not eliminate the stones completely. Still, it introduces patterns that do not exist in the original point cloud. Such an effect can also be seen at a sampling distance of 0.1 m. This is due to slight changes in the surface to the right of the specimen, causing higher volumetric density at some parts, which affects the downsampling. Application of the curvature-aware method retains the artifact, but the stones are lost at a 0.1-m sampling distance.

Saliency values in this dataset were computed with a 0.05-m minimal object size. For surface features estimation, occlusions dictated a neighborhood of at least 0.03 m.

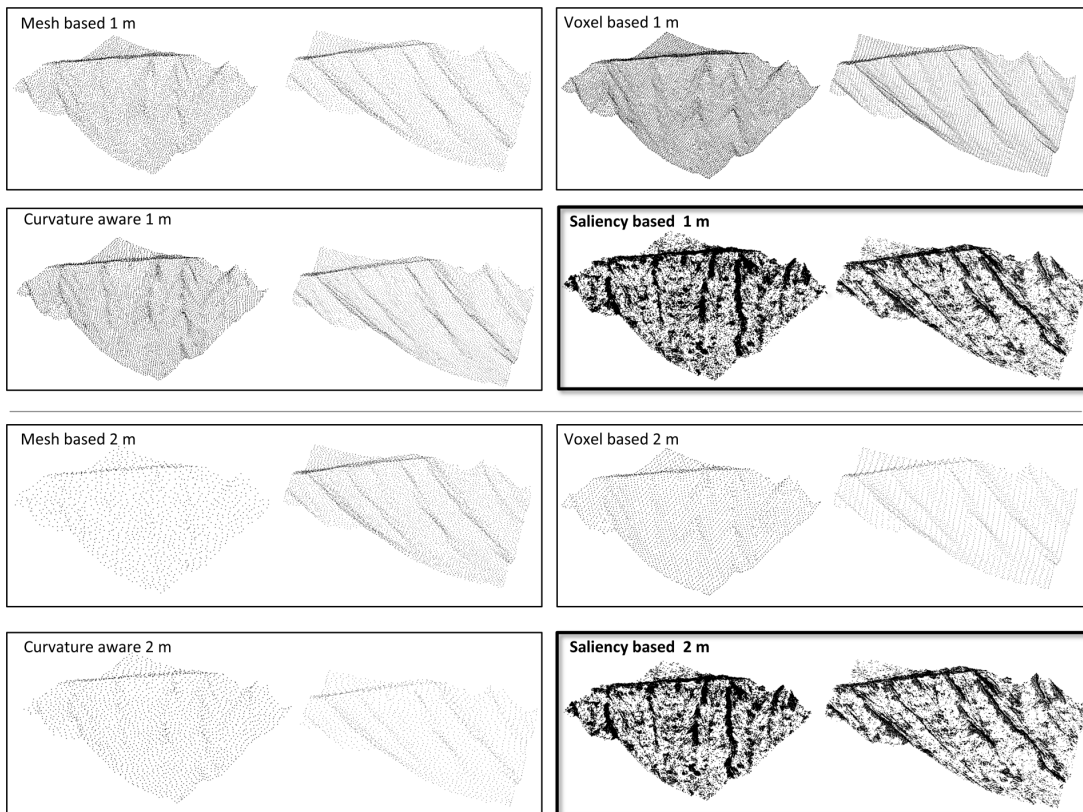


Fig. 9. Simplified point clouds of dataset #II (alpine terrain) using different methods and scales.

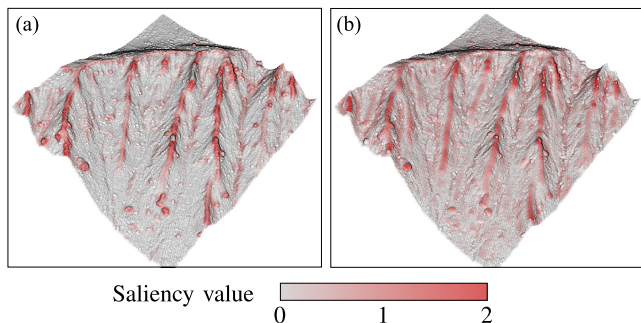


Fig. 10. Saliency estimation of dataset # II (alpine terrain) at (a) 1- and (b) 1.5-m object sizes.

The resulting simplified cloud shows the site’s stones remain intact (Fig. 12). This is achieved for all sampling distances with the proposed method. The flat terrain around the stones enables reduction rates of up to 95.8% without affecting the similarity to the original (Fig. 13). The reduction rate is lower than in other methods (95.1% on average). At a sampling distance of 1 m, 9393 points are left out of 224 186, compared to the 9, 16, and 11 points that are left after simplification with the mesh-based, voxel-based, and curvature-aware methods, respectively (Table IV). Clearly, these datasets after simplification are unusable. Note that in nonsalient regions, the reduction was similar to the curvature-aware method, pointing to good results in regions that are uninteresting.

Examination of the DoN distribution in the data shows that for all methods, most of the deviations are on the specimen’s

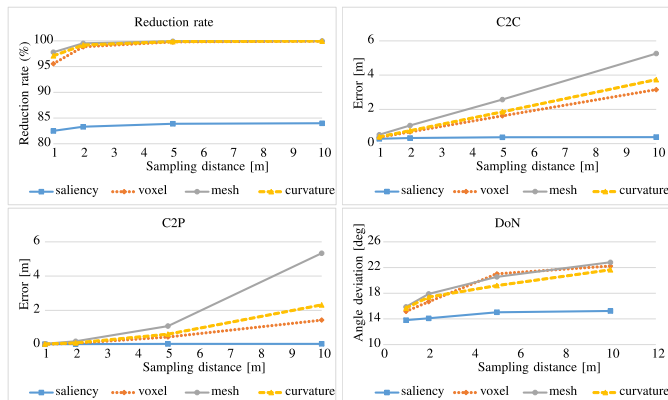


Fig. 11. Quantitative analysis of the simplification methods in different sampling distances in dataset #II (alpine terrain). The graphs of the C2C and C2P errors present the mean value of all errors; the DoN graphs show the median value.

stones and in their vicinity (Fig. 12). Nonetheless, in the proposed saliency-based point cloud, this deviation exists only along the higher stones. These stones create occlusions, which lead to biased normal estimations. Hence, following the reduction, these normals show a higher discrepancy.

The C2C and C2P distances in the saliency-based simplified clouds are close to zero for all reduction levels, where the C2P distance is less than a millimeter (Fig. 12). This is probably due to the generally flat nature of the dataset. The DoN is no higher than 0.8°. This is opposed to the other methods, which introduce at least 1.5° for the higher simplification levels.

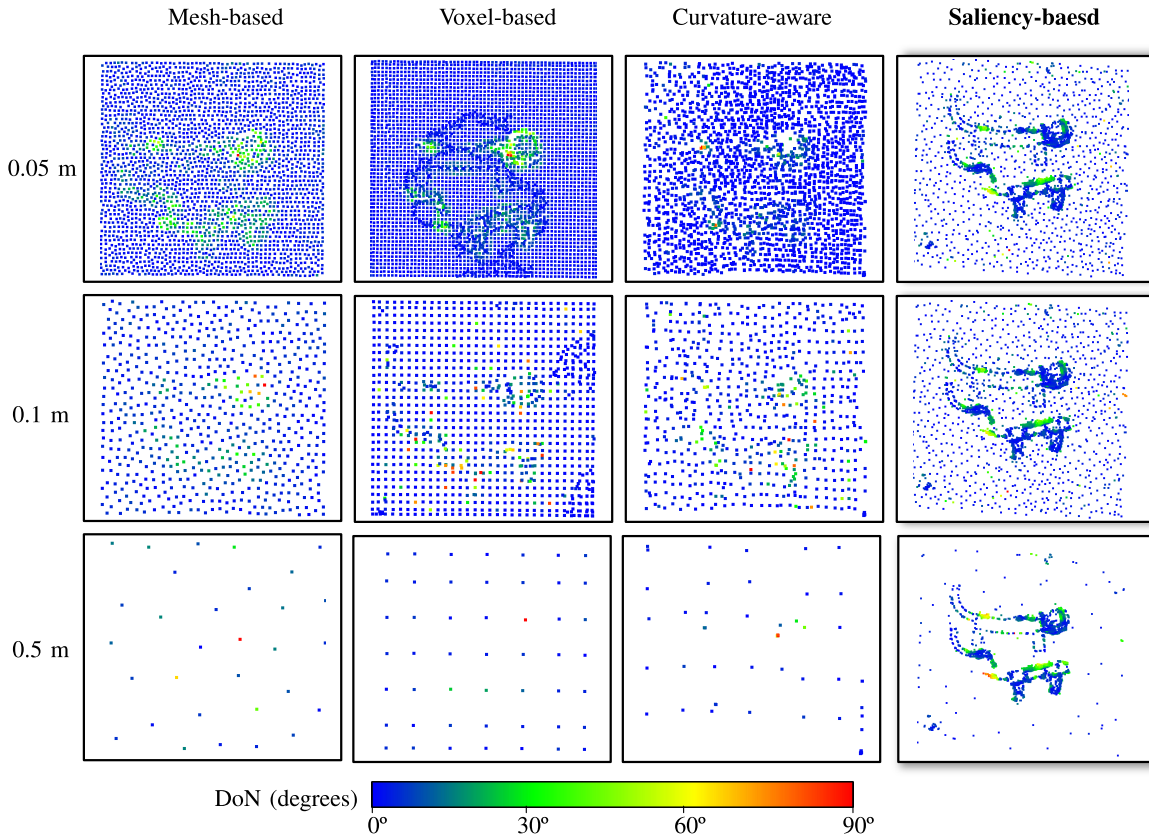


Fig. 12. Simplified point cloud of dataset #III (archeological site) using different methods and scales. Colors represent the angle of normal deviation from the original cloud. As almost no points were left at a 1-m sampling distance for the baseline methods, this level of simplification is not shown.

TABLE IV
NUMBER OF POINTS REMAINING IN DATASET #III
(ARCHEOLOGICAL SITE) AFTER REDUCTION

Sampling distance [m]	0.05	0.1	0.5	1
Saliency-based	13,045	11,361	9,572	9,393
Mesh-based	2,616	650	31	9
Voxel-based	4,158	1,091	49	16
Curvature-based	3,405	897	40	11

D. Dataset #IV—Cave

The last dataset was acquired terrestrially in the Untere Traisenbacher Höhle cave that is located on the steep northern slope of Ebenberg, Austria (see Table I and [47, Fig. 4]). This dataset is intended to test the proposed method in a full 3-D environment. A closed cave, with its walls and ceiling, provides such a complex scene. Inside the cave, small rocks are lying on the floor, and there are pockets and niches within the walls and ceiling [Fig. 4(d)]. A comprehensive morphological survey would require their detailed documentation, while the surface of the walls, floor, and ceiling is of less importance.

Saliency was computed with 0.3-m minimal object size, based on 0.1-m-radius neighbors for surface features

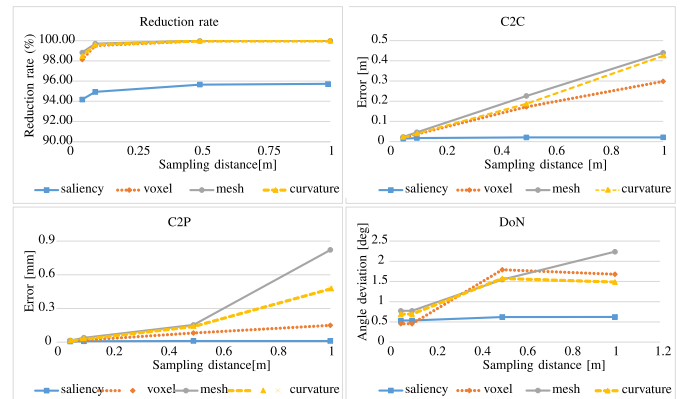


Fig. 13. Quantitative analysis of the simplification methods in different sampling distances in dataset #III (archeological site). The graphs of the C2C and C2P errors present the mean value of all errors; the DoN graphs show the median value.

estimation (Fig. 14). Blocks that are larger than the minimal object size are marked as salient, as well as the pockets and niches in the walls and ceiling [Fig. 14(a)]. At the back of the cave, the notches were also marked as salient [Fig. 14(b)]. Note that since the saliency is performed point-wise and according to the available neighborhood within a specific radius, the occluded regions did not affect the saliency estimation.

Next, we turn to the simplification phase. Due to the complexity of the dataset, a visual representation of the entire cave

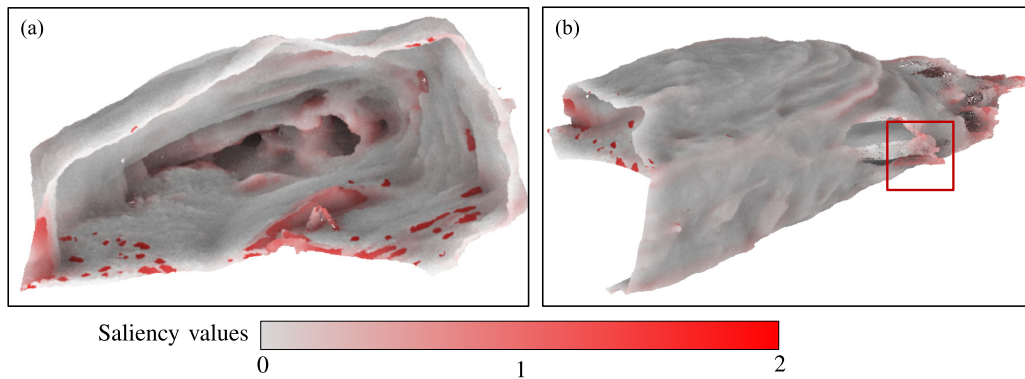


Fig. 14. Saliency estimation in dataset #IV (cave): (a) look from the entrance inside the cave and (b) look from the outside, showing niches and pockets that were detected by the saliency. The red rectangle marks the focus of Fig. 15.

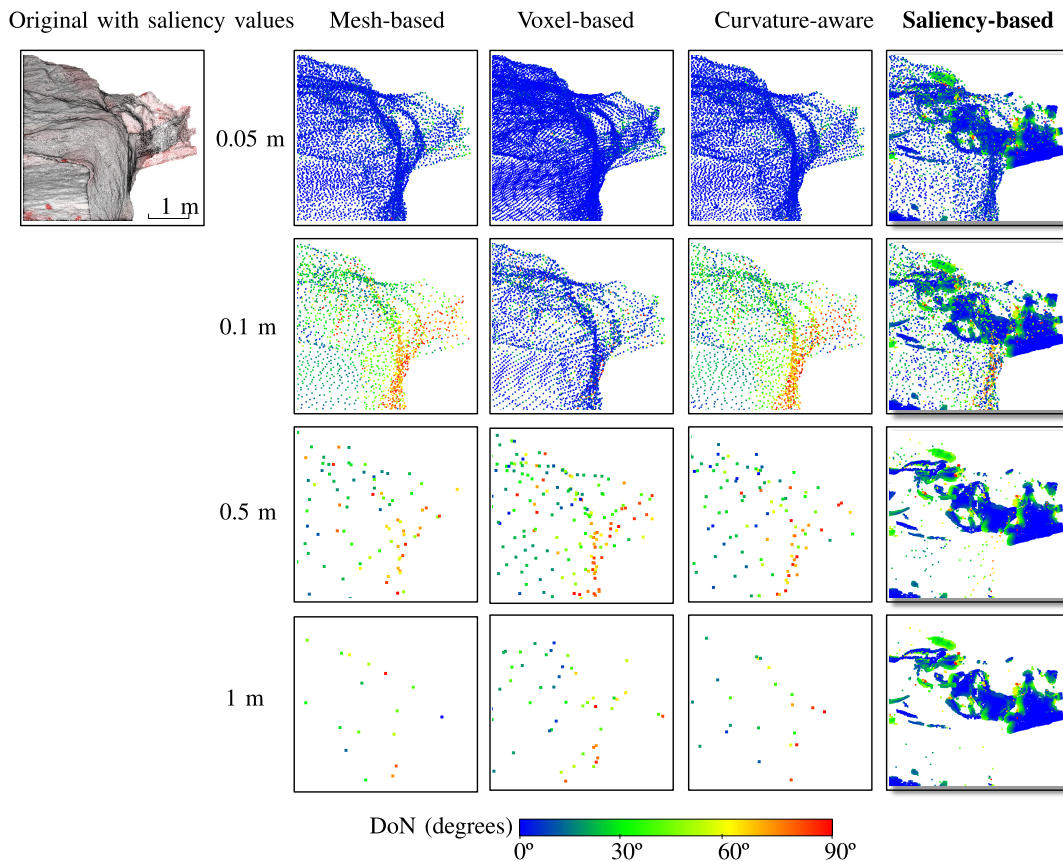


Fig. 15. Detail from the simplified point clouds of dataset #IV (cave) using different methods and scales. Colors represent the angle of normal deviation from the original cloud. Due to the complexity of the dataset, this is only a representative detail instead of the entire set [which is marked as a red rectangle in Fig. 14(b)].

after simplification was incomprehensible. While we analyze the results for the entire cave, we demonstrate them only on a specific detail [Fig. 15 (left)]. At 0.05- and 0.1-m sampling distances, the mesh-based, voxel-based, and curvature-aware models result in a smooth but detailed point cloud. However, at 0.5 and 0.1 m, the minute details disappear or change the entities' form. As an example, the length of the niche presented in (Fig. 15) shortens by 0.1–0.4 m between the original cloud and the various downsampled versions at these levels. This change of form does not occur in the proposed

saliency-based reduction, where both form and detail of the niche are consistent in all levels of simplification and only the wall surface is less detailed. Note also that for both curvature- and mesh-based methods, the normal estimations differ for the whole niche, while the voxel-based presents the lowest deviation from the original normals. However, in the saliency-based reduced point cloud, the normal discrepancies remain constant in the higher reduction rates, while the voxel-based (and the other methods) changes the surface completely. The C2C distances correspond to this fact (Fig. 16), where the

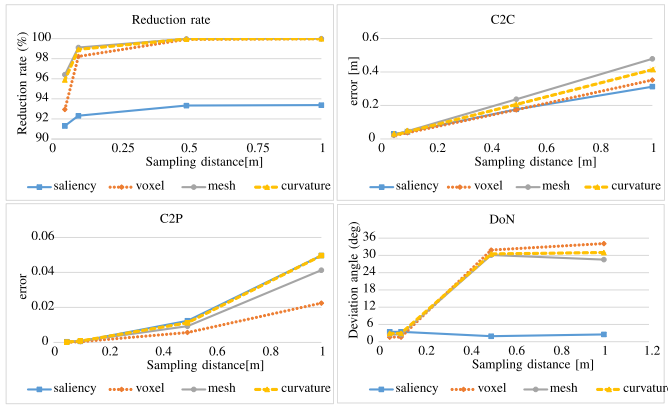


Fig. 16. Quantitative analysis of the simplification methods in different sampling distances in dataset #IV (cave). The graphs of the C2C and C2P errors present the mean value of all errors; the DoN graphs show the median value.

TABLE V
NUMBER OF POINTS REMAINING IN DATASET #IV
(CAVE) AFTER REDUCTION

Sampling distance [m]	0.05	0.1	0.5	1
Saliency-based	70,986	63,696	55,900	53,135
Mesh-based	28,218	6,995	261	64
Voxel-based	55,418	13,977	562	142
Curvature-based	32,301	8,436	345	87

saliency-based method produces the closest simplified cloud to the original (0.31 m). This is also true for the DoN angles, where the lowest variation is in the saliency-based simplified cloud, reaching up to 3.8°, as opposed to 24°, 22.8°, and 22.5° for the voxel-, mesh-, and curvature-based point clouds. Contrarily, the C2P distances of the proposed method are higher than those of the voxel-based and curvature-aware point clouds (0.4 versus 0.2 m, respectively). This can be attributed to the strong local surface variability. As in the previous datasets, the reduction rate of the proposed method is lower than that of the other methods, standing on 93.4% at the higher sampling distance (see Fig. 16 and Table V).

IV. CONCLUSION

In this article, we introduced a new point cloud simplification approach driven by saliency and executed by a hierarchical proximity data structure. Assuming that ROIs should be represented in higher resolution, we proposed to first evaluate the saliency of each point. Then, neighboring points are defined using a ball tree data structure, which is attuned to the surficial characteristics of laser scanning point clouds. The simplification is then carried out by choosing one representative point from each cell.

The application of the proposed method was tested on different scenarios, acquired by various laser scanners, at varying

resolutions. We have shown that point clouds simplified by our method enable the representation of important details even at high levels of reduction. We have also shown that the proposed method highlights ROIs by retaining more points there. We have shown that the saliency-based simplification results in point clouds that are more similar to the originals than those produced by other well-established methods.

It should be noted that the proposed simplification is less efficient in extreme changes in topography, where conspicuous regions are hard to define. Furthermore, the proposed method can be improved by defining a different scheme for retaining points, rather than a binary decision. Such an approach should consider both the magnitude of the saliency values and their nonsalient surroundings. Under such a model, differences in normal estimations may be reduced and some reduction can be made in salient regions.

REFERENCES

- [1] J. Telling, A. Lyda, P. Hartzell, and C. Glennie, "Review of Earth science research using terrestrial laser scanning," *Earth-Sci. Rev.*, vol. 169, pp. 35–68, Jun. 2017.
- [2] Y. Jo and S. Hong, "Three-dimensional digital documentation of cultural heritage site based on the convergence of terrestrial laser scanning and unmanned aerial vehicle photogrammetry," *ISPRS Int. J. Geo-Inf.*, vol. 8, no. 2, p. 53, Jan. 2019.
- [3] Y. Wang, Q. Chen, Q. Zhu, L. Liu, C. Li, and D. Zheng, "A survey of mobile laser scanning applications and key techniques over urban areas," *Remote Sens.*, vol. 11, no. 13, p. 1540, Jun. 2019.
- [4] A. Martínez-Fernández *et al.*, "3D monitoring of Paleolithic archaeological excavations using terrestrial laser scanner systems (Sierra de Atapuerca, railway trench sites, Burgos, n Spain)," *Digit. Appl. Archaeol. Cultural Heritage*, vol. 19, Dec. 2020, Art. no. e00156.
- [5] A. Guerin *et al.*, "Quantifying 40 years of rockfall activity in Yosemite valley with historical structure-from-motion photogrammetry and terrestrial laser scanning," *Geomorphology*, vol. 356, May 2020, Art. no. 107069.
- [6] G. Rilov, N. David, T. Guy-Haim, D. Golomb, R. Arav, and S. Filin, "Sea level rise can severely reduce biodiversity and community net production on rocky shores," *Sci. Total Environ.*, vol. 791, Oct. 2021, Art. no. 148377.
- [7] C.-K. Wang and N. Fareed, "Mapping drainage structures using airborne laser scanning by incorporating road centerline information," *Remote Sens.*, vol. 13, no. 3, p. 463, Jan. 2021.
- [8] M. Wojtkowska, M. Kedzierski, and P. Delis, "Validation of terrestrial laser scanning and artificial intelligence for measuring deformations of cultural heritage structures," *Measurement*, vol. 167, Jan. 2021, Art. no. 108291.
- [9] L. Guo *et al.*, "Extraction of dense urban buildings from photogrammetric and LiDAR point clouds," *IEEE Access*, vol. 9, pp. 111823–111832, 2021.
- [10] N. Leal, E. Leal, and S.-T. German, "A linear programming approach for 3D point cloud simplification," *IAENG Int. J. Comput. Sci.*, vol. 44, no. 1, pp. 60–67, 2017.
- [11] G. Wang, L. Wu, Y. Hu, and M. Song, "Point cloud simplification algorithm based on the feature of adaptive curvature entropy," *Meas. Sci. Technol.*, vol. 32, no. 6, Mar. 2021, Art. no. 065004.
- [12] D. P. Luebke, "A developer's survey of polygonal simplification algorithms," *IEEE Comput. Graphics Appl.*, vol. 21, no. 3, pp. 24–35, May/June 2001.
- [13] S.-M. Hur, H.-C. Kim, and S.-H. Lee, "STL file generation with data reduction by the Delaunay triangulation method in reverse engineering," *Int. J. Adv. Manuf. Technol.*, vol. 19, no. 9, pp. 669–678, May 2002.
- [14] M. Corsini, P. Cignoni, and R. Scopigno, "Efficient and flexible sampling with blue noise properties of triangular meshes," *IEEE Trans. Vis. Comput. Graphics*, vol. 18, no. 6, pp. 914–924, Jun. 2012.
- [15] C. Ji, Y. Li, J. Fan, and S. Lan, "A novel simplification method for 3D geometric point cloud based on the importance of point," *IEEE Access*, vol. 7, pp. 129029–129042, 2019.
- [16] K. Zhang, S. Qiao, X. Wang, Y. Yang, and Y. Zhang, "Feature-preserved point cloud simplification based on natural quadric shape models," *Appl. Sci.*, vol. 9, no. 10, p. 2130, May 2019.

- [17] R. B. Rusu and S. Cousins, "3D is here: Point cloud library (PCL)," in *Proc. IEEE Int. Conf. Robot. Autom.*, Shanghai, China, May 2011, pp. 1–4.
- [18] Q.-Y. Zhou, J. Park, and V. Koltun, "Open3D: A modern library for 3D data processing," 2018, *arXiv:1801.09847*.
- [19] (2021). *Cloudcompare*. [Online]. Available: <http://www.cloudcompare.org/>
- [20] L. Ma, T. Whelan, E. Bondarev, P. H. N. de With, and J. McDonald, "Planar simplification and texturing of dense point cloud maps," in *Proc. Eur. Conf. Mobile Robots*, Sep. 2013, pp. 164–171.
- [21] V. Morell, S. Orts, M. Cazorla, and J. Garcia-Rodriguez, "Geometric 3D point cloud compression," *Pattern Recognit. Lett.*, vol. 50, pp. 55–62, Dec. 2014.
- [22] Y.-J. Lin, R. R. Benziger, and A. Habib, "Planar-based adaptive down-sampling of point clouds," *Photogrammetric Eng. Remote Sens.*, vol. 82, no. 12, pp. 955–966, Dec. 2016.
- [23] T. Li, Q. Pan, L. Gao, and P. Li, "A novel simplification method of point cloud with directed Hausdorff distance," in *Proc. IEEE 21st Int. Conf. Comput. Supported Cooperat. Work Design (CSCWD)*, Apr. 2017.
- [24] M. Gong, Z. Zhang, and D. Zeng, "A new simplification algorithm for scattered point clouds with feature preservation," *Symmetry*, vol. 13, no. 3, p. 399, Feb. 2021.
- [25] W. Xuan, X. Hua, X. Chen, J. Zou, and X. He, "A new progressive simplification method for point cloud using local entropy of normal angle," *J. Indian Soc. Remote Sens.*, vol. 46, no. 4, pp. 581–589, Dec. 2017.
- [26] A. Mahdaoui and E. H. Sbai, "3D point cloud simplification based on the clustering algorithm and introducing the Shannon's entropy," in *13th Int. Conf. Mach. Vis.*, W. Osten, J. Zhou, and D. P. Nikolaev, Eds. Bellingham, WA, USA: SPIE, Jan. 2021, Art. no. 116050N.
- [27] R. Arav, "MorE3D version v0.0.3," TU Wien, LIC, MIT License, VCS, Aug. 2022. [Online]. Available: <https://github.com/TUW-GEO/MorE3D/>
- [28] M. Molenaar and T. Cheng, "Fuzzy spatial objects and their dynamics," *ISPRS J. Photogramm. Remote Sens.*, vol. 55, no. 3, pp. 164–175, Sep. 2000.
- [29] A. Stein, A. Dilo, A. Lucieer, and D. van de Vlag, "Definition and identification of vague spatial objects and their use in decision ontologies," in *Proc. 3rd Int. Symp. Spatial Data Qual. (ISSDQ)*, Bruck an der Leitha, Austria, A. Frank and E. Grum, Eds. Vienna, Austria: Technical Univ. of Vienna, Apr. 2004, pp. 99–115.
- [30] A. Dilo, R. A. de By, and A. Stein, "A system of types and operators for handling vague spatial objects," *Int. J. Geographical Inf. Sci.*, vol. 21, no. 4, pp. 397–426, Apr. 2007.
- [31] L. Itti, C. Koch, and E. Niebur, "A model of saliency-based visual attention for rapid scene analysis," *IEEE Trans. Pattern Anal. Mach. Intell.*, vol. 20, no. 11, pp. 1254–1259, Nov. 1998.
- [32] S. Frintrop, E. Rome, and H. I. Christensen, "Computational visual attention systems and their cognitive foundations," *ACM Trans. Appl. Perception*, vol. 7, no. 1, pp. 1–39, Jan. 2010.
- [33] R. Cong, J. Lei, H. Fu, M.-M. Cheng, W. Lin, and Q. Huang, "Review of visual saliency detection with comprehensive information," *IEEE Trans. Circuits Syst. Video Technol.*, vol. 29, no. 10, pp. 2941–2959, Oct. 2019.
- [34] R. Arav and S. Filin, "A visual saliency-driven extraction framework of smoothly embedded entities in 3D point clouds of open terrain," *ISPRS J. Photogramm. Remote Sens.*, vol. 188, pp. 125–140, Jun. 2022.
- [35] GEO, TU Wien. *OPALS—Orientation and Processing of Airborne Laser Scanning Data*. [Online]. Available: <https://opals.geo.tuwien.ac.at/html/2.4.0/index.html>
- [36] Z. Shtain and S. Filin, "Hierarchical proximity-based over-segmentation of 3-D point clouds for efficient graph feature detection," *ISPRS Ann. Photogramm., Remote Sens. Spatial Inf. Sci.*, vol. 2, pp. 273–280, Aug. 2020.
- [37] F. Pedregosa *et al.*, "Scikit-learn: Machine learning in Python," *J. Mach. Learn. Res.*, vol. 12, no. 10, pp. 2825–2830, Jul. 2017.
- [38] P. Cignoni, M. Callieri, M. Corsini, M. Dellepiane, F. Ganovelli, and G. Ranzuglia, "MeshLab: An open-source mesh processing tool," in *Proc. 6th Eurographics Italian Chapter Conf.*, 2008, pp. 129–136. [Online]. Available: <http://vcg.isti.cnr.it/Publications/2008/CCDGR08>
- [39] D. Tian, H. Ochimizu, C. Feng, R. Cohen, and A. Vetro, "Geometric distortion metrics for point cloud compression," in *Proc. IEEE Int. Conf. Image Process. (ICIP)*, Sep. 2017, pp. 3460–3464.
- [40] Geological Survey of Israel and R. Arav, "Zeelim fan, Israel (part)," TU Data Repository, 2013, doi: [10.48436/mps0m-c9n43](https://doi.org/10.48436/mps0m-c9n43).
- [41] Y. Avni *et al.*, "Self-accelerated development of salt Karst during flash floods along the dead sea coast, Israel," *J. Geophys. Res., Earth Surf.*, vol. 121, no. 1, pp. 17–38, Jan. 2016, doi: [10.1002/2015jf003738](https://doi.org/10.1002/2015jf003738).
- [42] M. Shviro, I. Haviv, and G. Baer, "High-resolution InSAR constraints on flood-related subsidence and evaporite dissolution along the Dead Sea shores: Interplay between hydrology and rheology," *Geomorphology*, vol. 293, pp. 53–68, Sep. 2017, doi: [10.1016/j.geomorph.2017.04.033](https://doi.org/10.1016/j.geomorph.2017.04.033).
- [43] A. Ronen, M. Ezersky, A. Beck, B. Gatenio, and R. B. Simhayov, "Use of GPR method for prediction of sinkholes formation along the dead sea shores, Israel," *Geomorphology*, vol. 328, pp. 28–43, Mar. 2019, doi: [10.1016/j.geomorph.2018.11.030](https://doi.org/10.1016/j.geomorph.2018.11.030).
- [44] M. Abelson, "Hydrological and geological controls on the evolution of the dead sea sinkholes," in *The Many Facets of Israel's Hydrogeology* (Springer Hydrogeology). Cham, Switzerland: Springer, Nov. 2020, pp. 273–298, doi: [10.1007/978-3-030-51148-7_15](https://doi.org/10.1007/978-3-030-51148-7_15).
- [45] R. Arav, S. Filin, and Y. Avni, "Sinkhole swarms from initiation to stabilisation based on *in situ* high-resolution 3-D observations," *Geomorphology*, vol. 351, Feb. 2020, Art. no. 106916, doi: [10.1016/j.geomorph.2019.106916](https://doi.org/10.1016/j.geomorph.2019.106916).
- [46] "Kauertal dataset (part)," Photogrammetry Research Group, TU Wien, TU Data Repository, 2017, doi: [10.48436/ft23-kvr16](https://doi.org/10.48436/ft23-kvr16).
- [47] M. Wimmer and P. Oberender, "Untere traisenbacher höhle—UTB_104423," TU Data Repository, 2022, doi: [10.48436/fh0am-at738](https://doi.org/10.48436/fh0am-at738).



Reuma Arav received the B.Sc., M.Sc., and Ph.D. degrees in mapping and geoinformation engineering from the Technion—Israel Institute of Technology, Haifa, Israel, in 2010, 2013, and 2020, respectively.

She is currently an Individual Research Fellow at the Photogrammetry Research Group, Technische Universität Wien (TU Wien), Vienna, Austria, under the Marie-Sklodowska-Curie Actions.



Sagi Filin received the B.Sc. and M.Sc. degrees in geodetic engineering from the Technion—Israel Institute of Technology (IIT), Haifa, Israel, in 1989 and 1995, respectively, and the Ph.D. degree in geodetic sciences from The Ohio State University, Columbus, OH, USA, in 2001.

From 2001 until 2004, he was with the Photogrammetry and Remote Sensing Section, Delft University of Technology, Delft, The Netherlands. Since 2004, he has been a Faculty Member with the Department of Transportation and Geo-Information Engineering, Faculty of Civil and Environmental Engineering, Technion—IIT.



Norbert Pfeifer received the Dipl.Ing. and Ph.D. degrees in surveying engineering from Technische Universität Wien (TU Wien), Vienna, Austria, in 1997 and 2002, respectively.

He was an Assistant Professor with the Delft University of Technology and a Senior Researcher with the alp-S, Centre of Natural Hazard Management, Innsbruck, Austria. He is currently a Professor of photogrammetry with the Department of Geodesy and Geoinformation, TU Wien. His research interests include topographic and 3-D modeling, laser

scanning, automatic scene reconstruction, and the exploitation of point clouds in environmental sciences.

Dr. Pfeifer is a member of the International Society of Photogrammetry and Remote Sensing.